Electronic Supplementary Material (ESI) for Nanoscale.
This journal is © The Royal Society of Chemistry 2023

Electronic Supplementary Information

3D Surface Nanomechanical Properties Mapping Method with a Magnetic-drive Orthogonal Cantilever Probe

Junyuan Geng[a,b], Hao Zhang*[a], Xianghe Meng[a] and Hui Xie*[a]

[a]State key Laboratory of Robotics and Systems, School of Mechatronics Engineering, Harbin Institute of Technology, Harbin 150080, PR China.

[b]Institute of Robotics and Automatic Information System and the Tianjin Key Laboratory of Intelligent Robotic, Nankai University, Tianjin 300350, China.

*Corresponding authors: haoz@hit.edu.cn (Hao Zhang) and xiehui@hit.edu.cn (Hui Xie).

I. Three working modes of 3D FD-AFM:

There are three working modes of bending, torsion and vector tracking in the proposed three-dimensional force-distance curve-based atomic force microscopy (3D FD-AFM) method to achieve two-dimensional (2D) horizontal surface mapping, 2D sidewall mapping and continuous 3D surface mapping, respectively. Comprehensive scanning protocols of these three working modes have been described as follows:

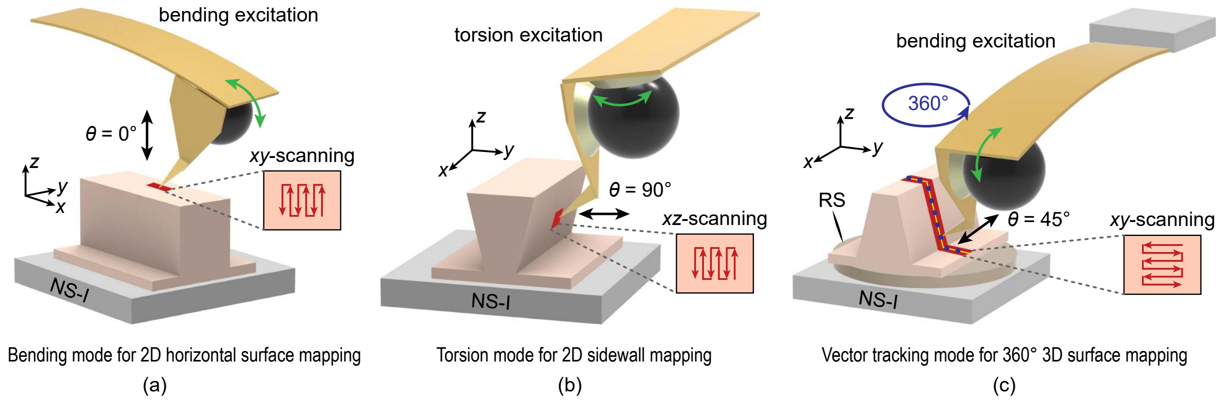

Figure S 1. Three working modes of 3D FD-AFM: (a) bending mode for 2D horizontal surface mapping, (b) torsion mode for 2D sidewall mapping and (c) vector tracking mode for 360° 3D surface mapping.

Bending mode for 2D horizontal surface mapping

- Scanning in xy plane and displacement compensation along the z-axis are set. Bending excitation is selected and the deflection of the magnetic-drive orthogonal cantilever probe (MD-OCP) is used as the feedback to regulate position coordinates of the nanopositioning stage-I (NS-I). The vector angle θ is determined to be 0°.
- Move the interested position to the center of top-view, and coarsely adjust the xy position coordinates with the NS-I. Real-time imaging and scanning will be executed afterwards.

Torsion mode for 2D sidewall mapping

- Scanning in xz plane and displacement compensation along the y-axis are set. Torsion excitation is selected and the torsional deformation of MD-OCP is used as the feedback to regulate position coordinates of the NS-I. The vector angle θ is determined to be 90°.

- Move the interested position to the center of top-view and coarsely adjust the *xy* position coordinates with the NS-I. As for deep sidewalls, the tip is controlled to contact the top of the detected structure at first, so as to determine the limit coordinate along the *z*-axis during sidewall scanning. As for nanoscale sidewalls, the tip should contact on the top and bottom of the detected structure in order to determine the effective scanned range along the *z*-axis.
- Move the interested position to the center of side-view, and coarsely adjust the *xz* position coordinates with the NS-I. Real-time imaging and scanning will be executed subsequently, during which the *z*-axis coordinate should be guaranteed within the scannable height range.

Vector tracking mode for 360° 3D surface mapping

- Scanning in *xy* plane and displacement compensation in *yz* plane are set. Bending excitation is selected and the deflection of MD-OCP is used as the feedback. The vector angle θ is determined to be 45° (or another customized angle). The displacement errors are divided into two parts to be compensated: *z*-axis displacement of the NS-I and *y*-axis displacement of the nanopositioning stage-II (NS-II). To avoid the influence of laser movement along the *y*-axis, an amplitude compensation method[1] is adopted during scanning.
- Move the interested position to the center of top-view and coarsely adjust the *xy* position coordinates with the NS-I. Real-time imaging and scanning will be executed, and then rotate the sample by a certain angle with the help of the rotation stage (RS), which should ensure that there is enough overlap between the next scanning area and the previous one. A home positioning method[2] is used to bring the target sample to its original center after every rotation. Subsequently, another set of the same operations will be repeated.
- The scan will end after completing the whole 360° characterization of the target sample. An omnidirectional 3D imaging of the topography and nanomechanical properties can be realized. If necessary, the imaging results can be stitched and reconstructed based on the overlap.

II. Measurement principle of SNMP:

Surface nanomechanical properties (SNMP) can be deduced from FD curves as shown in **Figure S2**. At the beginning of an approach-retract cycle, the tip approaches the sample, controlled by the attractive force (F_{att}). As the distance x_{dis} decreases, the repulsive force (F_{rep}) appears and gradually counteracts F_{att}. When the F_{rep} reaches the set peak force (Point A), approaching is over and the tip begins to withdraw from the sample. The F_{rep} gradually decreases to zero during retraction. Due to surface adhesion, negative deformation is generated, which can be reset to zero until the elastic recovery force of probe is large enough to overcome the adhesion (Point B). SNMP mapping can be achieved by analysis of FD curves in each approach-retract periods during scanning.

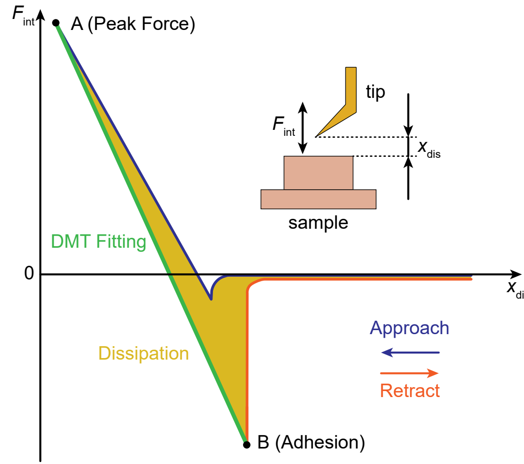

Figure S 2. Analysis of the FD curve obtained during tip-sample interaction.

The MD-OCP vibrates at a low frequency during SNMP measurement, meanwhile, it is constrained by inertial, damping, interaction and driving forces. According to the Euler-Bernoulli beam theory, the dynamic equation of MD-OCP can be expressed as follows[3,4]:

$$m\ddot{z} + \frac{m\omega_0}{Q}\dot{z} + kz = F_{int} + F_d \cos(\omega_d t) \quad \textbf{(S1)}$$

where m, ω_0, and k are the equivalent mass, resonance frequency and spring constant of probe, respectively. Q is the quality factor. F_d and ω_d are the amplitude and frequency of driving force. F_{int} is the interaction force between tip and sample. z is the detected cantilever deformation.

To dissociate F_{int} from **Equation** (S1), it is necessary to evaluate the unloaded motion state of MD-OCP without interaction, the dynamic equation of which can

be expressed as follows:

$$m\ddot{z}_0 + \frac{m\omega_0}{Q}\dot{z}_0 + kz_0 = F_\mathrm{d}\cos(\omega_\mathrm{d}\mathrm{t}) \tag{S2}$$

where z_0 is the detected cantilever deformation without interaction.

During low frequency drive, the inertial force and damping force can be ignored[5]. The interaction force can be deduced as follows according to the difference between **Equation** (S1) and (S2)[6,7]:

$$k(z - z_0) = F_\mathrm{int} \tag{S3}$$

Equation (S3) can be further expressed as follows:

$$\frac{k(U_\mathrm{load} - U_\mathrm{free})}{S} = F_\mathrm{int} \tag{S4}$$

where S is the system sensitivity, U_load and U_free are the loaded and unloaded voltages reflecting the deformation of the MD-OCP, respectively.

As illustrated in **Figure S**2, topography imaging can be realized by compensating the peak force at point A with feedback. The adhesion (F_adh) can be deduced through the following expression[7]:

$$F_\mathrm{adh} = \frac{kU_\mathrm{adh}}{S} \tag{S5}$$

where U_adh is the output voltage at the maximum negative force point B in FD curves.

The effective Young's modulus of sample (E^*) can be obtained after fitting the data of retraction phase between point A and B using the Derjaguin-Muller-Toporov (DMT) model[8,9]:

$$F_\mathrm{in} - F_\mathrm{adh} = \frac{4}{3}E^*\sqrt{R_\mathrm{p}\delta^3} \tag{S6}$$

where R_p is the tip radius and δ is the sample deformation.

The total stiffness (k_total) during indentation ($F_\mathrm{int} > 0$) can be determined as follows:

$$k_\mathrm{total} = \frac{kU_\mathrm{peak}}{x_\mathrm{inden}S} \tag{S7}$$

where U_peak is the output voltage at peak point A in FD curves, x_inden is the probe displacement during indentation.

While the sample stiffness k_s can be deduced as follows:

$$k_\mathrm{s} = \frac{k k_\mathrm{total}}{k - k_\mathrm{total}} \tag{S8}$$

The energy dissipation (E_diss) in each cycle can be acquired by integrating the hysteresis area between the approach and retract curves, which can be expressed as follows[10]:

$$E_\mathrm{diss} = \oint \overrightarrow{F_\mathrm{int}} \mathrm{d}\overrightarrow{x_\mathrm{dis}} = \int_0^T \overrightarrow{F_\mathrm{int}} \cdot \overrightarrow{v_\mathrm{dis}} \mathrm{d}t \tag{S9}$$

where $\overrightarrow{F_\mathrm{int}}$ is the interaction force vector, $\overrightarrow{x_\mathrm{dis}}$ and $\overrightarrow{v_\mathrm{dis}}$ are the displacement and velocity vector of the probe respectively, T is the approach-retract cycle time.

III. SEM Images of MD-OCPs:

The horizontal cantilever and vertical cantilever with the protruding tip of MD-OCP were separately prepared by milling two commercial probes (HQ:NSC18/Al-BS, MikroMasch, USA; and ATEC-FM, Nanosensors, Switzerland) using the focused ion beam (FIB) technology (FIB/SEM dual beam system, Helios NanoLab 600i, FEI Company, USA). And then, one selected ferromagnetic bead with its diameter similar to the width of the horizontal cantilever was adhered to the free end of the horizontal cantilever using epoxy adhesive (A-05HP, Angeluo, China). Finally, the horizontal cantilever and vertical cantilevers were assembled by gluing[11], and the prepared MD-OCP can be obtained. The vertical cantilever made from ATEC-FM with a typical AFM tip radius of 10 nm fully guarantees high measurement resolution[12–14].

Figure S3 shows the scanning electron microscope (SEM) images of MD-OCPs. The ferroferric oxide bead of MD-OCP I is magnetized along the long axis of its horizontal cantilever, while the ferroferric oxide bead of MD-OCP II is magnetized along the direction perpendicular to the long axis of its horizontal cantilever.

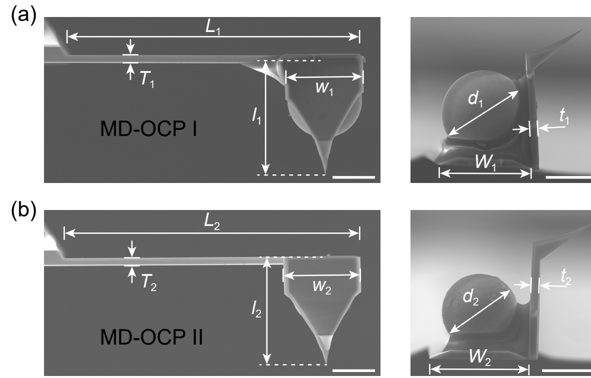

Figure S 3. SEM images of two MD-OCPs: (a) MD-OCP I is used under bending excitation mode and (b) MD-OCP II is used under torsion excitation mode. Scale bars: 20 μm.

In the MD-OCP I, the length (L_1), width (W_1) and thickness (T_1) of the horizontal cantilever are determined as 137.31 μm, 36.49 μm and 3.2 μm, respectively, the length (l_1), width (w_1) and thickness (t_1) of the vertical cantilever are determined as 53.31 μm, 35.80 μm and 3.2 μm, respectively, the diameter of the micro bead (d_1) is 33.76 μm. In the MD-OCP II, the length (L_2), width (W_2) and thickness (T_2) of the horizontal cantilever are determined as 138.58 μm, 36.66 μm and 3.1 μm, respectively, the length (l_2), width (w_2) and thickness (t_2) of the vertical cantilever are determined as 50.17 μm, 35.76 μm and 3.0 μm, respectively, the

diameter of the micro bead (d_2) is 25.49 μm. The tip radiuses of the MD-OCP I and MD-OCP II are both determined as 10 nm.

IV. Calibration of the Spring Constant:

Spring constant of MD-OCP indicates relationship between the detected micro-cantilever deformation and the interaction force, which is necessary to be calibrated before SNMP measurements.

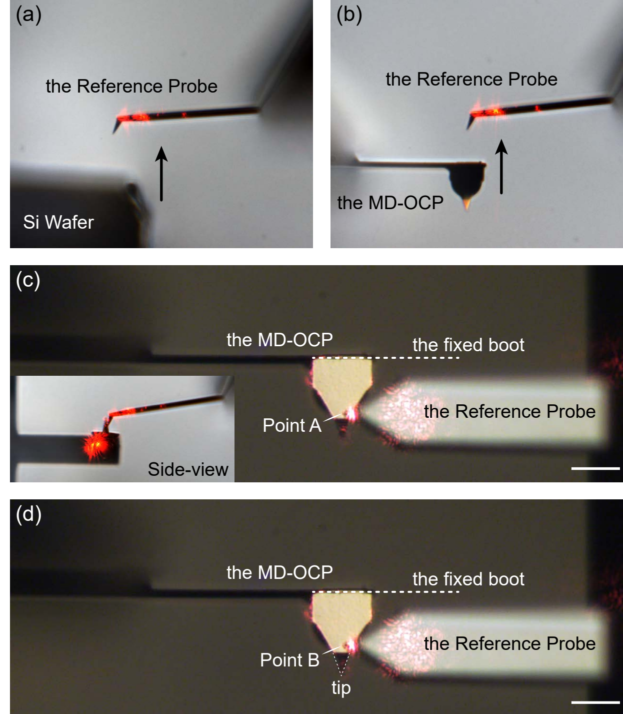

Figure S 4. Optical images of the spring constant calibration process. (a) Contact on the silicon wafer. (b) Contact on the horizontal cantilever end of MD-OCP during bending spring constant calibration. (c) Contact at point A on the vertical cantilever of MD-OCP during torsion spring constant calibration with a side-view in the inset. (d) Contact at point B on the vertical cantilever of MD-OCP during torsion spring constant calibration. Scale bar: 30 μm.

Calibration of bending spring constant was performed using the reference probe method[15]: a standard commercial probe with known spring constant (PPP-NCHR, Nanosensors, k_r=47.6 N/m) was used to make contact on a clean silicon wafer and the horizontal cantilever end of the calibrated MD-OCP, as shown in **Figure S**4(a) and (b). And then, a further approaching of about 300 nm between the standard probe and the detected surface was achieved through lifting the NS-I. The correlation curves between the output voltage and distance was obtained as shown in **Figure S**5(a). According to these calibration curves, the bending spring constant (k_b) of MD-OCP I can be determined as 27.76 N/m by

the following formula[11]:

$$k = \left(\frac{S_{\text{cal}}}{S_{\text{hard}} - S_{\text{cal}}} \right) k_{\text{r}} \quad \text{(S10)}$$

where k is the spring constant to be measured, S_{hard} and S_{cal} are the fitting results of sensitivities acquired on the hard silicon wafer and the horizontal cantilever end, respectively, k_{r} is the bending spring constant of the standard probe.

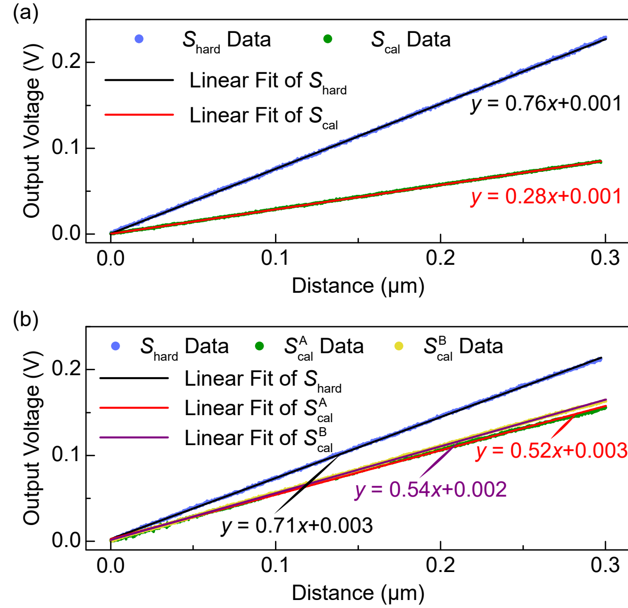

Figure S 5. Calibration curves with linear fit results of (a) the bending spring constant and (b) the torsion spring constant.

The torsion spring constant calibration procedure based on the reference method is mostly the same as above-described, except that the corresponding point on the calibrated probe should theoretically be located at the tip, but two points (A and B) were selected on the vertical cantilever to protect the tip from damage, as shown in **Figure S**4(c) and (d). The calibration curves have been illustrated in **Figure S**5(b), from which the torsion spring constants at points A (k_{t}^{A}) and B (k_{t}^{B}) can be determined as 130.27 N/m and 151.20 N/m respectively according to **Equation** (S10). Based on the optical microscopy images in which one pixel represents 0.33 μm, the distance from the fixed root of vertical cantilever to the tip (l), points A (l_{b}^{A}) and B (l_{b}^{B}) have been determined as 50.17 μm, 34.00 μm and 31.00 μm, respectively. The torsion spring constant at the tip (k_{t}) of MD-OCP II

can be determined as 57.47 N/m by the following expressions:

$$\frac{k_{\mathrm{bA}}^{\mathrm{v}}}{k_{\mathrm{bB}}^{\mathrm{v}}} = \left(\frac{l_{\mathrm{b}}^{\mathrm{B}}}{l_{\mathrm{b}}^{\mathrm{A}}}\right)^{3} \tag{S11}$$

$$\frac{k_{\mathrm{b}}^{\mathrm{v}}}{k_{\mathrm{bA}}^{\mathrm{v}}} = \left(\frac{l_{\mathrm{b}}^{\mathrm{A}}}{l}\right)^{3} \tag{S12}$$

$$\frac{1}{k_{\mathrm{b}}^{\mathrm{v}}} + \frac{1}{k_{\mathrm{t}}^{\mathrm{h}}} = \frac{1}{k_{\mathrm{t}}} \tag{S13}$$

$$\frac{1}{k_{\mathrm{bA}}^{\mathrm{v}}} + \frac{1}{k_{\mathrm{t}}^{\mathrm{h}}} = \frac{1}{k_{\mathrm{t}}^{\mathrm{A}}} \tag{S14}$$

$$\frac{1}{k_{\mathrm{bB}}^{\mathrm{v}}} + \frac{1}{k_{\mathrm{t}}^{\mathrm{h}}} = \frac{1}{k_{\mathrm{t}}^{\mathrm{B}}} \tag{S15}$$

where $k_{\mathrm{t}}^{\mathrm{h}}$ is the torsion spring constant of horizontal cantilever, $k_{\mathrm{b}}^{\mathrm{v}}$, $k_{\mathrm{bA}}^{\mathrm{v}}$ and $k_{\mathrm{bB}}^{\mathrm{v}}$ are the bending spring constants of vertical cantilever at the tip, points A and B, respectively.

V. Calibration of the System Sensitivity:

System sensitivity is another crucial parameter to be calibrated, which reflects relationship between the output voltage and the detected microcantilever deformation. Unifying related system sensitivities via appropriate adjustment of laser spot location facilitates derivation of displacement, probe deformation and indentation, etc.

During magnetic-drive SNMP measurement under bending excitation mode, the torque-induced deflection curve of the horizontal cantilever is different from the force-induced deflection curve, which means that there are two deflection sensitivities (S_M^b and S_F^b) need to be calibrated[16]. During magnetic-drive SNMP characterization under torsion excitation mode, the torque-induced torsion curve and the force-induced torsion curve are similar when the vertical cantilever can be considered as rigid body.

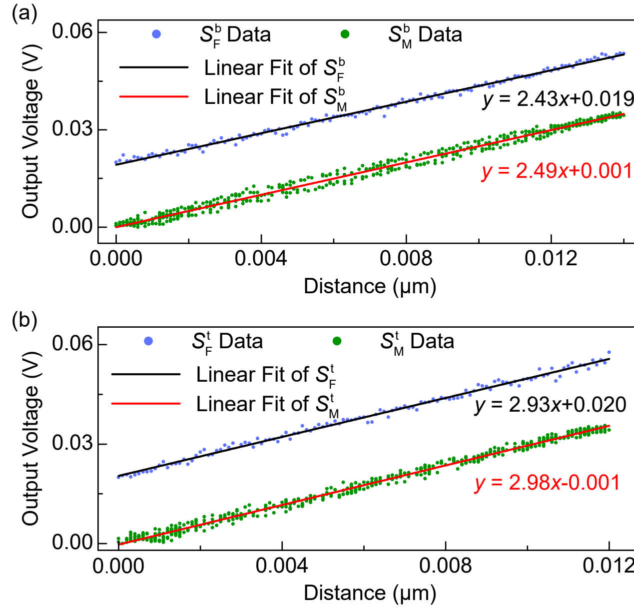

Figure S 6. Calibration curves with linear fit results of (a) deflection sensitivities and (b) torsion sensitivities. 0.02 V was added to the output voltage of S_F^b and S_F^t to separate two sets of data in each subfigures.

Laser spot location adjustment can make the S_M^b and S_F^b tend to be the same[6]. The final calibrated results have been shown in **Figure S**6(a) in which 0.02 V was added to the output voltage of S_F^b to separate two sets of data. It can be obtained that the error between S_M^b and S_F^b is reduced less than 5% after repeated adjustments.

The torque-induced torsion sensitivity (S^{t}_{M}) and the force-induced torsion sensitivity (S^{t}_{F}) were calibrated as demonstrated in **Figure S6**(b). An extra 0.02 V was also added to the output voltage of S^{t}_{F} for clear distinction in **Figure S6**(b). Linearity fitting results show that the error between S^{t}_{M} and S^{t}_{F} is only 2%, thus these two system sensitivities can be considered to be consistent.

According to the mean values of the torque-induced and the force-induced sensitivities, the final system sensitivities under bending (S_{b}) and torsion excitations (S_{t}) were determined as 2.46 V/μm and 2.96 V/μm, respectively.

VI. Supplementary Experimental Data and Images:

Table S 1. Statistical results of the critical dimensions of the microarray unit.

No.	I	II	III	IV	V	Mean
α (°)	56.27	57.63	58.61	60.30	58.52	58.26±1.48
H (μm)	2.04	2.04	2.03	2.03	2.03	2.03±0.01

Table S 2. Statistical data of 2D surface mapping results

	R_q(nm)	F_{adh} (nN)	E^* (GPa)	k_s (N/m)	E_{diss} (keV)
Top	7.63	497.90±144.95	2.20±0.53	42.41±7.71	82.73±15.59
Bottom	5.44	340.05±136.82	2.06±0.37	41.07±4.64	12.20±8.94
Sidewall	20.69	386.38±112.29	4.10±2.85	64.88±62.80	207.27±148.06

Table S 3. Statistical results based on the marked lines in 2D surface mapping images

	R_q(nm)	F_{adh} (nN)	E^* (GPa)	k_s (N/m)	E_{diss} (keV)
Top	6.71±0.98[#]	507.17±52.74	2.10±0.14	41.34±1.02	82.41±6.92
Bottom	3.59±0.73	329.30±39.65	2.06±0.07	41.09±0.56	11.50±5.48
Sidewall	11.17±4.28	376.13±95.63	4.52±1.91	67.63±23.33	120.28±124.26

[#]All standard deviations are calculated based on three averages along marked lines

Table S 4. Statistical data of 3D surface mapping results

	A	B	C	D	Total
F_{adh} (nN)	454.54±123.36	455.71±103.65	482.28±102.91	434.38±104.12	459.14±109.02
E^* (GPa)	3.09±1.74	2.95±1.64	3.08±1.69	3.23±1.88	3.09±1.74
k_s (N/m)	57.98±23.08	56.26±21.79	55.19±20.10	55.40±21.68	56.02±21.50
E_{diss} (keV)	105.18±31.97	97.90±31.87	79.34±16.76	57.51±36.74	83.47±34.07

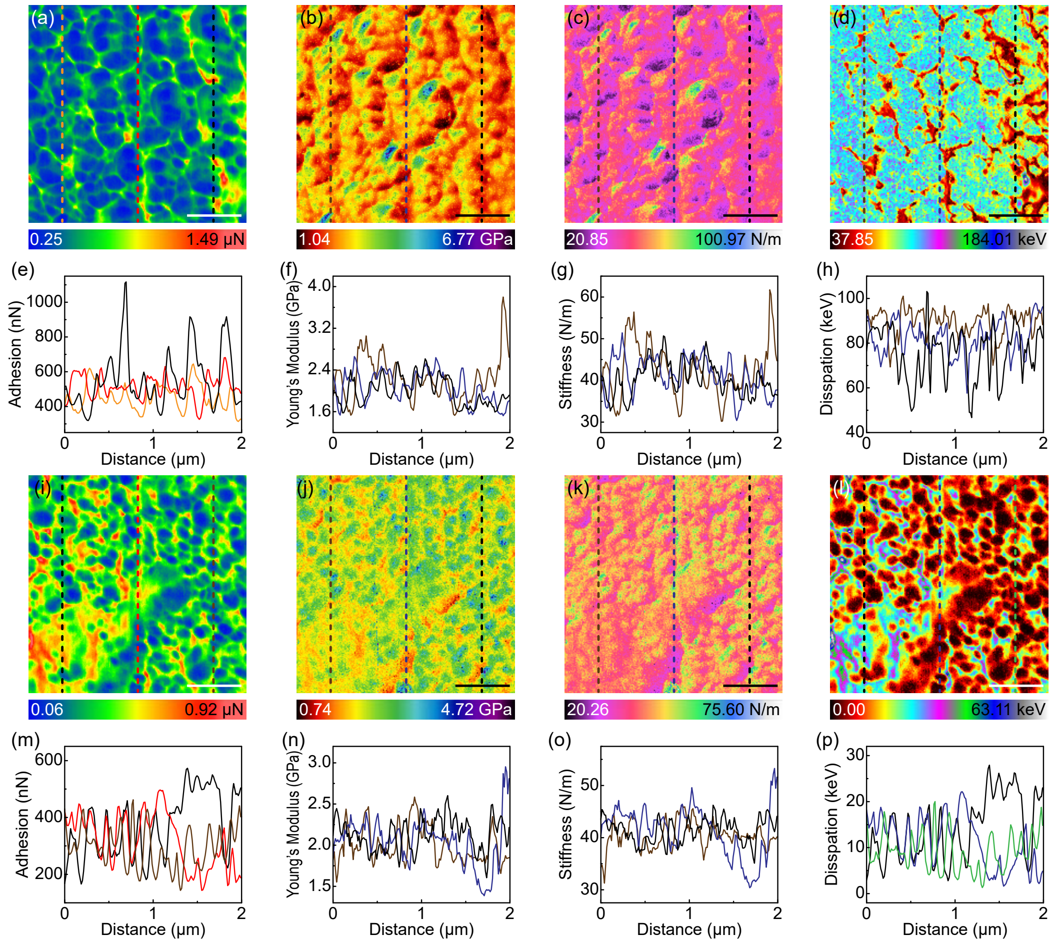

Figure S 7. SNMP mapping results of the 2D horizontal surfaces of the microarray unit. (a)-(d) and (i)-(l) are the images of F_{adh}, E^{*}, k_{s} and E_{diss} obtained on the top and bottom. (e)-(h) and (m)-(p) are the corresponding profiles along the marked lines in (a)-(d) and (i)-(l), respectively.

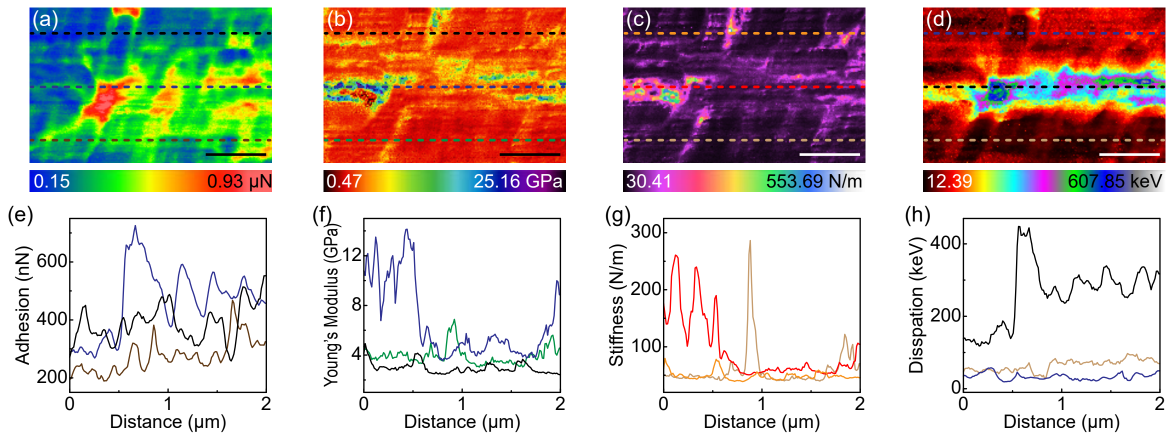

Figure S 8. SNMP mapping results of the 2D sidewall of the microarray unit. (a)-(d) are the sidewall images of F_{adh}, E^{*}, k_{s} and E_{diss}, respectively. (e)-(h) are the corresponding profiles along the marked lines in (a)-(d).

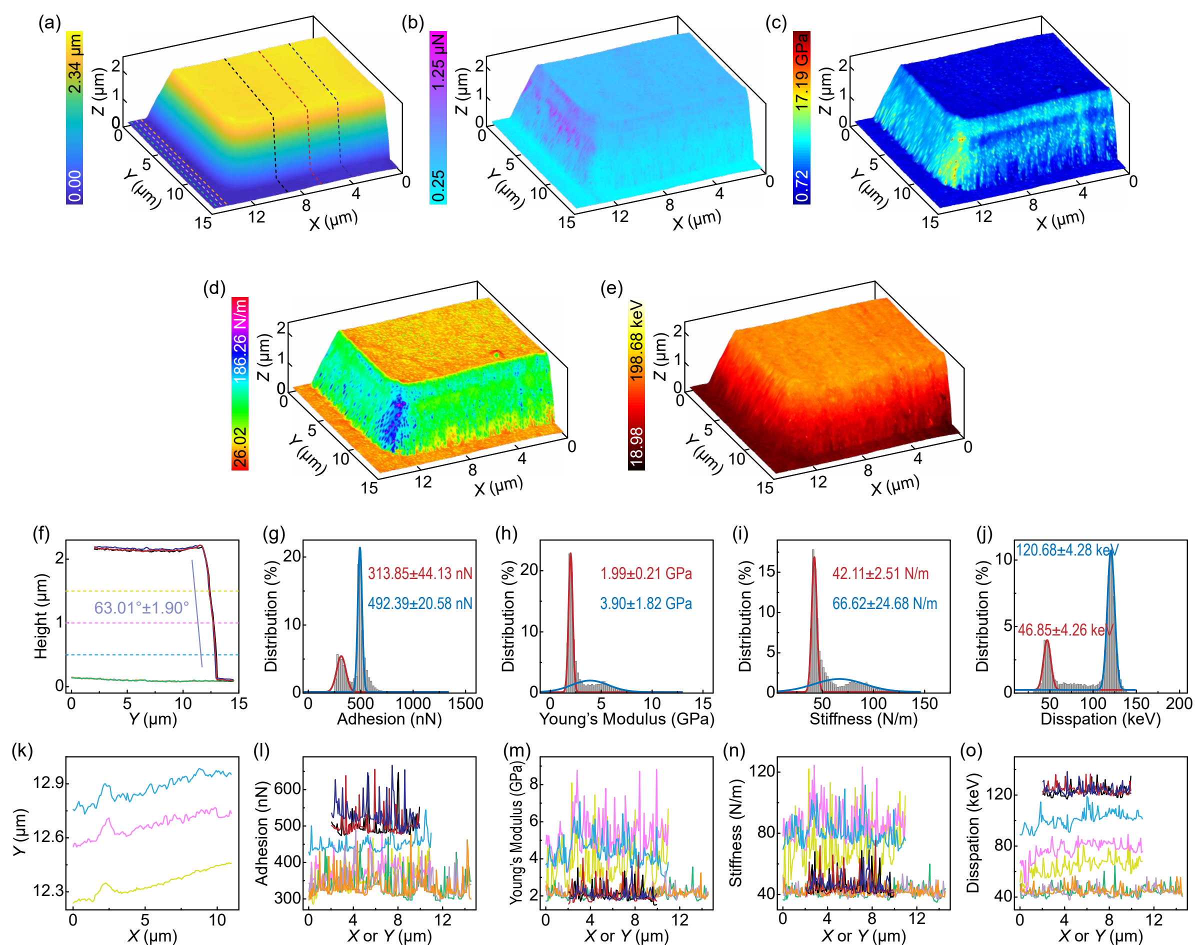

Figure S 9. 3D surface mapping results of the microarray unit acquired at the rotation angle of 90°, $X \times Y$ range: 15.1 μm×14.6 μm. (a)-(e) are 4D images in which the color bars represent height, F_{adh}, E^*, k_s and E_{diss}, respectively. (f) is the height profiles along the indicated lines in (a). (g)-(j) are the statistical histograms with Gaussian fitting results corresponding to the SNMP images in (b)-(e). (k) is the cross-section profiles along the dotted lines in (f). (l)-(o) are the sectional SNMP profiles of (b)-(e) along the dotted lines in (f) and indicated lines in (a).

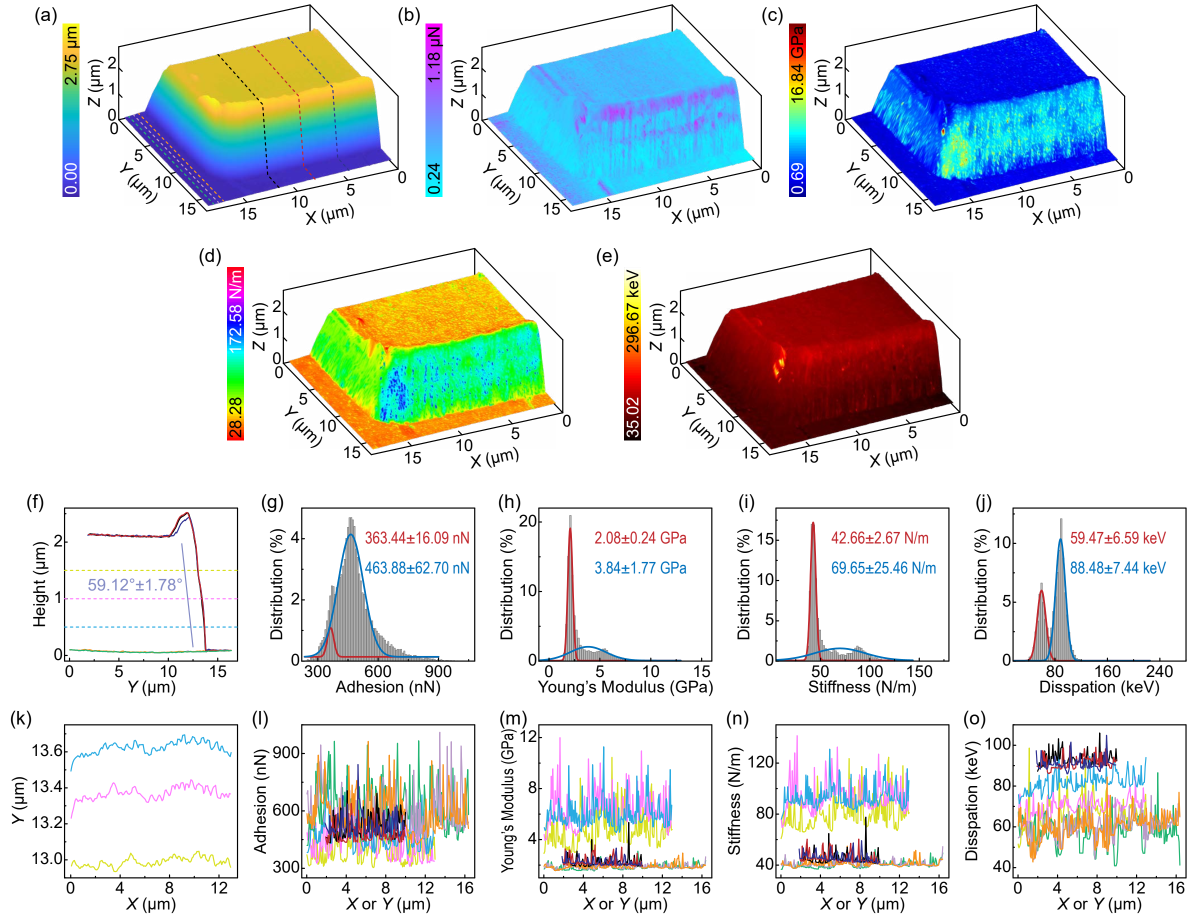

Figure S 10. 3D surface mapping results of the microarray unit acquired at the rotation angle of 180°, $X \times Y$ range: 18.5 μm×16.4 μm. (a)-(e) are 4D images in which the color bars represent height, F_{adh}, E^*, k_{s} and E_{diss}, respectively. (f) is the height profiles along the indicated lines in (a). (g)-(j) are the statistical histograms with Gaussian fitting results corresponding to the SNMP images in (b)-(e). (k) is the cross-section profiles along the dotted lines in (f). (l)-(o) are the sectional SNMP profiles of (b)-(e) along the dotted lines in (f) and indicated lines in (a).

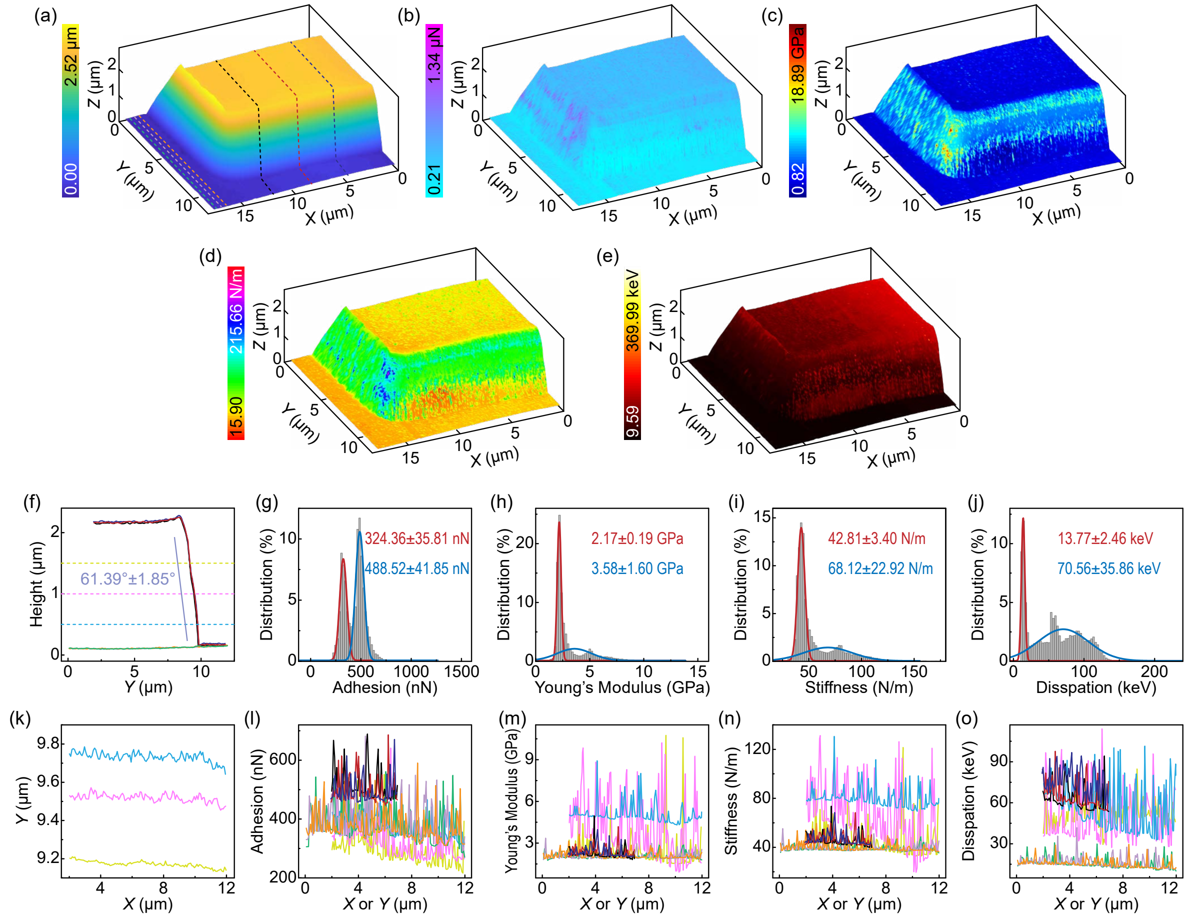

Figure S 11. 3D surface mapping results of the microarray unit acquired at the rotation angle of 270°, $X \times Y$ range: 17.9 μm$\times$12.0 μm. (a)-(e) are 4D images in which the color bars represent height, F_{adh}, E^*, k_{s} and E_{diss}, respectively. (f) is the height profiles along the indicated lines in (a). (g)-(j) are the statistical histograms with Gaussian fitting results corresponding to the SNMP images in (b)-(e). (k) is the cross-section profiles along the dotted lines in (f). (l)-(o) are the sectional SNMP profiles of (b)-(e) along the dotted lines in (f) and indicated lines in (a).

Reference

1. H. Xie, D. Hussain, F. Yang, and L. Sun, “Development of three-dimensional atomic force microscope for sidewall structures imaging with controllable scanning density,” IEEE-ASME Trans. Mechatron., vol. 21, no. 1, pp. 316–328, Feb 2016.

2. H. Lu, Y. Wen, H. Zhang, H. Xie, and Y. Shen, “360° multiparametric imaging atomic force microscopy: A method for three-dimensional nanomechanical mapping,” Ultramicroscopy, vol. 196, pp. 83–87, Jan 2019.

3. J. R. Lozano and R. Garcia, “Theory of phase spectroscopy in bimodal atomic force microscopy,” Phys. Rev. B, vol. 79, no. 1, p. 014110, Jan 2009.

4. A. San Paulo and R. Garcia, “Tip-surface forces, amplitude, and energy dissipation in amplitude-modulation (tapping mode) force microscopy,” Phys. Rev. B, vol. 64, no. 19, p. 193411, Nov 2001.

5. C. A. Amo and R. Garcia, “Fundamental high-speed limits in single-molecule, single-cell, and nanoscale force spectroscopies,” ACS nano, vol. 10, no. 7, pp. 7117–7124, Jul 2016.

6. X. Meng, H. Zhang, J. Song, Y. Wen, L. Sun, and H. Xie, “Simultaneously measuring force and displacement: Calibration of magnetic torque actuated microcantilevers for nanomechanical mapping,” IEEE Sens. J., vol. 18, no. 7, pp. 2682–2689, Apr 2018.

7. J. Geng, S. Li, H. Zhang, X. Meng, H. Gao, and H. Xie, “Characterization of topography and adhesion of sidewall using an orthogonal cantilever probe,” in 3M-NANO. IEEE, Aug 2021, pp. 431–436.

8. B. V. Derjaguin, V. M. Muller, and Y. P. Toporov, ”Effect of contact deformations on the adhesion of particles,” J. Colloid Interf. Sci., vol. 53, no. 2, pp. 314–326, Apr 1975.

9. Y. Wen, H. Lu, Y. Shen, and H. Xie, ”Nanorobotic manipulation system for 360° characterization atomic force microscopy,” IEEE Trans. Ind. Electron., vol. 67, no. 4, pp. 2916–2924, Apr 2020.

10. B. Pittenger, N. Erina, and C. Su, ”Quantitative mechanical property mapping at the nanoscale with PeakForce QNM,” Bruker Application Note, vol. 128, pp. 1–12, 2009.

11. J. Geng, H. Zhang, X. Meng, W. Rong, and H. Xie, ”Sidewall imaging of microarray-based biosensor using an orthogonal cantilever probe,” *IEEE Trans. Instrum. Meas.*, vol. 70, pp. 1–8, Mar 2021.

12. C. Xie, C. Mu, J. R. Cox, and J. M. Gerton, ”Tip-enhanced fluorescence microscopy of high-density samples,” *Appl. Phys. Lett.*, vol. 89, pp. 143117, Oct 2006.

13. J. Qu, M. Lee, M. Hilke, and X. Liu, ”Investigating the impact of SEM chamber conditions and imaging parameters on contact resistance of in situ nanoprobing,” *Nanotechnology*, vol. 28, pp. 345702, Jul 2017.

14. K. Kang, K. Godin, Y. D. Kim, S. Fu, w. Cha, J. Hone, and E. H. Yang, ”Graphene-assisted antioxidation of tungsten disulfide monolayers: substrate and electric-field effect,” *Adv. Mater.*, vol. 29, pp. 1603898, Feb 2017.

15. M. L. Palacio and B. Bhushan, ”Normal and lateral force calibration techniques for AFM cantilevers,” *Crit. Rev. Solid State Mat. Sci.*, vol. 35, no. 2, pp. 73–104, Jun 2010.

16. B. J. Goodno and J. M. Gere, Mechanics of Materials. Boston, MA, USA: Cengage Learning, 2020.